IEEJ Journal of Industry Applications
Vol.8 No.1 pp.131–139 DOI: 10.1541/ieejjia.8.131

Paper

Effectiveness of Convolutional Perfectly Matched Layer in Time-domain Numerical Analysis of Low-frequency Wireless Power Transfer

Hiroki Ishida* Member, Tomoaki Kyoden** Member
Hiroto Furukawa*** Member

(Manuscript received May 23, 2018, revised Sep. 4, 2018)

In this study, the absorption boundary conditions (ABCs) in electromagnetic field numerical analysis were investigated to improve the estimation accuracy of the magnetic coupling coefficient (k) for wireless power transfer (WPT). When using Berenger's perfectly matched layer (B-PML), the estimation accuracy of the k value was higher than that obtained using Mur's ABC. However, in the low-frequency band, at around 400 Hz, the magnetic field was not sufficiently attenuated in the absorption layer. There was also a problem with numerical stability. To solve these problems, we introduce the convolutional perfectly matched layer (C-PML). In this study, we propose a simple Debye distribution function as the matrix coefficient of the stretch coordinate metric. As a result, it was possible to evolve from B-PML to C-PML simply by adding a proportional coefficient γ. With the introduction of C-PML, the magnetic field was sufficiently attenuated in the absorption layer, and the numerical stability dramatically improved. C-PML is thus useful for low-frequency WPT simulation.

Keywords: wireless power transmission, FDTD method, super low frequency, convolutional perfectly matched layer

1. Introduction

Improving robustness has become a major research topic in wireless power transfer (WPT) [1]–[4]. For instance, in order to study WPT for electric vehicles (EVs) moving at high speed, dynamic electromagnetic field analysis in the time domain is necessary. However, few studies have investigated the dynamic changes in a magnetic field around coils. Time-domain analysis, which is suitable for investigating transient responses, is commonly conducted using the finite-difference time-domain method (FDTD) method [5]–[7]. In simulations such as electric motors, the finite element method (FEM) and the method of moments are commonly used for frequency-domain analysis [8][9]. Since FDTD has both space and time resolution restrictions [10], the number of iterations of numerical calculations is high for simulations in the terahertz and kilohertz bands, resulting in long calculation times [11]. Hence, FDTD has not been applied to the analysis of power electronics devices driven at sub-kilohertz frequencies. To overcome this limitation, the present study conducts an electromagnetic field analysis at sub-kilohertz frequencies using parallel computation with multiple graphics processing units (GPUs) [12][13].

* Department of Applied Physics, Okayama University of Science
1-1, Ridai-cho, Kita-ku, Okayama 700-0005, Japan
** National Institute of Technology, Toyama College, Imizu Campus
1-2, Ebie-neriya, Imizu, Toyama 933-0293, Japan
*** National Institute of Technology, Toyama college, Hongo Campus
13, Hongo-machi, Toyoma city, Toyama 939-8630, Japan

In WPT simulations, it is important to apply an absorption boundary condition (ABC) at the edges of the analysis area. The non-radiative magnetic field generated by a transmission coil spreads out in free space, and thus it is necessary to accurately analyze the magnetic field around coils. Safety standards for magnetic flux density exposure have been proposed by the International Commission on Non-Ionizing Radiation Protection (ICNIRP) [14]. Highly accurate calculation of the magnetic field around a device is needed to confirm these safety standards in the design stage.

Frequencies of about 85 kHz are generally used for magnetic resonance WPT for EVs. At such low frequencies, even if an ABC is not introduced at the edges of an analysis area, the influence of reflected waves will be almost negligible. However, if no ABCs are introduced, then the magnetic field will be cut off at the edges. Thus, part of the magnetic flux emitted from one pole of a magnetic dipole cannot return to the pole pair. In such a system, since Gauss's law does not hold, calculation results will be inaccurate.

Berenger's perfectly matched layer (B-PML) is a commonly used ABC in FDTD [15]. Its absorption performance is superior to that of other methods [16]–[18] and it has thus been widely adopted in simulations, such as those of microwave antennas and radar [19][20]. FDTD can be used to analyze non-radiative magnetic fields; however, it is known that B-PML has a drawback in the near field [21]. To overcome this drawback, B-PML has been modified to have Debye frequency dispersion characteristics [22][23]. ABCs in WPT simulations were studied by Sugahara [24], who simulated magnetic resonance WPT in the 13.56 MHz band based on FEM. In one study [24], the performance of the improvised absorbing boundary condition was compared with that of the

complex-frequency-shifted PML (CFS-PML), with the former shown to have better transmission efficiency. The present study simulates WPT using FDTD. The frequencies used here are below 85 kHz, and even super-low frequencies of about 400 Hz are used. Since the application of FDTD for WPT is relatively new [25][26], there are no previous reports on the corresponding ABCs.

2. Berenger's PML and Simulation Results

Simulation results obtained with B-PML are first discussed. Then, convolutional PML (C-PML) is proposed to solve the problems encountered with B-PML. To determine the effect of PML type, the magnetic coupling coefficient (k) was used as a quantitative index. If the boundary condition is set appropriately, then it is expected that the calculated magnetic field around the coils will be accurate, and thus the estimation of the k value will also be accurate. The transmission efficiency is strongly influenced by the product of the k value and the quality factor (Q) of the coil [27][28]. Accurately calculating the k value thus allows accurate calculation of efficiency.

Yee lattices cells were arranged in a two-dimensional (2D) analysis area, as shown in Fig. 1. Here, the length of a Yee cell in the x direction is Δx, and that in the y direction is Δy. Both Δx and Δy were set to 1.0 mm. The numbers of lattice cells in the x and y directions (N_x and N_y) were set to 736 and 672, respectively, for a maximum area of 768 × 768. Here, the analysis area includes an absorption layer. The size limit of the analysis area is determined by the number of CUDA cores (stream processors) and the amount of GPU memory. Two recent high-end GPUs (Nvidia GTX 1080 Ti) were used in this study. Without GPUs, a wider analysis area can be set, but an enormous amount of computation time will be needed, significantly reducing the practicality of the simulator. Detailed calculation time data are given in our previous report [12]. Another report showed that GPUs can be used to accelerate FDTD solvers [29].

As shown in Fig. 1, the coordinates of an intersection of

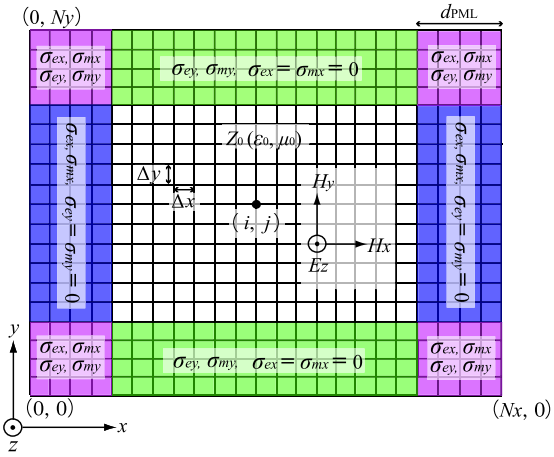

Fig. 1. PML arranged in 2D analysis area. For a propagating wave along the x direction arriving at either the right or left PML, since it is not necessary to attenuate the electric and magnetic fields in the y direction, the values of σ_{ey} and σ_{my} are set to zero. The inverse relationship holds for a propagating wave along the y direction

any lattice cells are expressed as $(x, y) = (i, j)$, and the electric field intensity in the z direction at these coordinates is expressed as $E_z(i, j)$. The magnetic field intensities on the x-y plane are expressed as $H_x(i, j)$ and $H_y(i, j)$. Here, the coordinates (i, j) indicate the intersection of the i-th cell in the x direction and the j-th cell in the y direction from the origin (0, 0). The magnetic and electric field intensities at arbitrary coordinates were calculated using the Ampere-Maxwell equation and Faraday's law, respectively, which were differentiated with respect to both space and time. To implement Yee algorithms in the WPT simulation, a book on FDTD simulation written by Uno [30] was consulted.

In this study, the thickness of the PML (d_{PML}) was set in the range of 4 to 96 layers. Assuming that the PML is an anisotropic material, the electric conductivity σ_e and magnetic conductivity σ_m in the PML are divided into two components in the x and y directions, respectively. When the impedance-matching condition is satisfied, the following relationships hold between electric conductivity and magnetic conductivity:

$$\begin{cases} \dfrac{\sigma_{mx}}{\mu_0} = \dfrac{\sigma_{ex}}{\varepsilon_0} \\ \dfrac{\sigma_{my}}{\mu_0} = \dfrac{\sigma_{ey}}{\varepsilon_0} \end{cases} \cdots\cdots (1)$$

Consider a parallel polarized transverse magnetic (TM) wave propagating in the 2D analysis area. The wave equations satisfying Eq. (1) are as follows:

$$\varepsilon_0 \frac{\partial E_{zx}}{\partial t} + \sigma_{ex} E_{zx} = \frac{\partial H_y}{\partial x} \cdots\cdots (2)$$

$$\varepsilon_0 \frac{\partial E_{zy}}{\partial t} + \sigma_{ey} E_{zy} = -\frac{\partial H_x}{\partial y} \cdots\cdots (3)$$

$$\mu_0 \frac{\partial H_x}{\partial t} + \sigma_{my} H_x = -\frac{\partial E_z}{\partial y} \cdots\cdots (4)$$

$$\mu_0 \frac{\partial H_y}{\partial t} + \sigma_{mx} H_y = \frac{\partial E_z}{\partial x} \cdots\cdots (5)$$

where E_z is divided into subcomponents E_{zx} and E_{zy} in consideration of the directions of the propagating wave ($E_z = E_{zx} + E_{zy}$). Differentiating these wave equations with respect to space and time, to follow Yee's scheme [31], yields Eqs. (6) to (9). For example, the magnetic field in the x direction at an arbitrary time ($t = n\Delta t$) and arbitrary position ($i\Delta x$, $j\Delta y$) was expressed as $H_x^n(i, j)$. The time step (Δt) was set to 1.92×10^{-12} s according to the Courant-Friedrichs-Lewy condition [10]. Note that σ_e and σ_m gradually increase until they reach the end of the PML, gradually attenuating the electromagnetic wave inside the PML. In general, σ_e and σ_m values are set to be proportional to the N-th power with respect to distance. The N value was set in the range of 2 to 8. It is also necessary to preset the amplitudes of σ_e and σ_m ($\sigma_{e,max}$ and $\sigma_{m,max}$, respectively). Therefore, the B-PML parameters that must be initially set are d_{PML}, N, and $\sigma_{e,max}$, whereas the $\sigma_{m,max}$ value should satisfy Eq. (1) and was set automatically in the simulation. The relationship between the $\sigma_{e,max}$ and the accuracy of numerical calculation $|\dot{R}|$ is as follows:

$$\sigma_{ex,max} = -\frac{N+1}{2Zd_{PML}} \ln |\dot{R}| \cdots\cdots (10)$$

where Z is the wave impedance of an analysis area. Since

$$E_{zx}{}^{n+1}(i,j) = \left(1+\frac{\sigma_{ex}(i)}{2\varepsilon_0}\Delta t\right)^{-1}\left[\left(1-\frac{\sigma_{ex}(i)}{2\varepsilon_0}\Delta t\right)E_{zx}{}^{n}(i,j)+\frac{\Delta t}{\varepsilon_0\Delta x}\left(H_y{}^{n+\frac{1}{2}}\left(i+\frac{1}{2},j\right)-H_y{}^{n+\frac{1}{2}}\left(i-\frac{1}{2},j\right)\right)\right] \cdots\cdots (6)$$

$$E_{zy}{}^{n+1}(i,j) = \left(1+\frac{\sigma_{ey}(j)}{2\varepsilon_0}\Delta t\right)^{-1}\left[\left(1-\frac{\sigma_{ey}(j)}{2\varepsilon_0}\Delta t\right)E_{zy}{}^{n}(i,j)-\frac{\Delta t}{\varepsilon_0\Delta y}\left(H_x{}^{n+\frac{1}{2}}\left(i,j+\frac{1}{2}\right)-H_x{}^{n+\frac{1}{2}}\left(i,j-\frac{1}{2}\right)\right)\right] \cdots\cdots (7)$$

$$H_x{}^{n+\frac{1}{2}}\left(i,j+\frac{1}{2}\right) = \left(1+\frac{\sigma_{my}(j+\frac{1}{2})}{2\mu_0}\Delta t\right)^{-1}\left[\left(1-\frac{\sigma_{my}(j+\frac{1}{2})}{2\mu_0}\Delta t\right)H_x{}^{n-\frac{1}{2}}\left(i,j+\frac{1}{2}\right)-\frac{\Delta t}{\mu_0\Delta y}(E_z{}^{n}(i,j+1)-E_z{}^{n}(i,j))\right] \cdots\cdots (8)$$

$$H_y{}^{n+\frac{1}{2}}\left(i+\frac{1}{2},j\right) = \left(1+\frac{\sigma_{mx}(i+\frac{1}{2})}{2\mu_0}\Delta t\right)^{-1}\left[\left(1-\frac{\sigma_{mx}(i+\frac{1}{2})}{2\mu_0}\Delta t\right)H_y{}^{n-\frac{1}{2}}\left(i+\frac{1}{2},j\right)+\frac{\Delta t}{\mu_0\Delta x}(E_z{}^{n}(i+1,j)-E_z{}^{n}(i,j))\right] \cdots\cdots (9)$$

we use single-precision floating-point operations in the numerical calculations, $|\dot{R}|$ should be above 10^{-7} for all calculation conditions. According to Eq. (10), when $\sigma_{e,max}$ is above 10^{-4} S/m, the required accuracy is satisfied. Therefore, in this study, $\sigma_{e,max}$ was set in the range of 10^{-4} to 10^{2} S/m.

For the left PML in the analysis area, there is the relationship of Eq. (11) between these parameters.

$$\begin{cases}\sigma_{ex} = \sigma_{ex,max}\left(\dfrac{d_{\mathrm{PML}}-i\Delta x}{d_{\mathrm{PML}}}\right)^{N}\\ \sigma_{mx} = \sigma_{mx,max}\left(\dfrac{d_{\mathrm{PML}}-i\Delta x}{d_{\mathrm{PML}}}\right)^{N}\end{cases} \cdots\cdots (11)$$

Curves of σ_{ex} with respect to distance ($i\Delta x$) in the x direction for various d_{PML} values are shown in Fig. 2. According to Eq. (11), the magnitude of σ_{ex} is asymptotic to the horizontal axis at the boundary. The general overview of the electromagnetic wave inside the PML is as follows: when the wave penetrates into the PML from the boundary, it gradually attenuates as σ_{ex} gradually increases, and then it approaches zero before it reaches the end of the PML. However, if σ_{ex} rapidly increases (e.g., blue curves for $d_{\mathrm{PML}} = 8$ in Fig. 2), then the situation becomes similar to that in which the analysis area is surrounded by metal walls. On the other hand, if σ_{ex} increases very slowly when d_{PML} is higher, then the PML may sufficiently perform its function. However, a thick PML significantly increases computation time. Therefore, it is necessary to find the minimum PML thickness necessary to achieve the required accuracy.

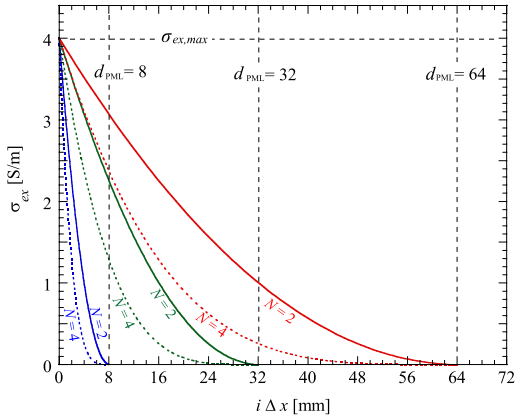

Fig. 2. Curves of σ_{ex} inside PML with respect to distance ($i\Delta x$) in x direction. Curves for $d_{\mathrm{PML}} = 8$, 32, and 64 are shown in blue, green, and red, respectively. Solid and broken-line curves are for $N = 2$ and 4, respectively. In this graph, $\sigma_{ex,max}$ was fixed at 4.0 S/m

For comparison with measurement results, the prototype (P6) shown in Fig. 3(a) was simulated. Our device was designed to be driven at about 400 Hz to realize WPT through a metal plate (see Fig. 3(b)). Specifications of P6 are given in Table 1. All numerical values shown in the table are measured values.

Before showing the simulation results for P6, we would like to explain the significance of calculating the k value using time-domain analysis. The formula for transmission efficiency (η) was derived from an equivalent circuit [25] and is expressed as follows:

$$\eta = \frac{1}{1+\dfrac{2}{k\sqrt{Q_1Q_2}}+\dfrac{2r_c(k+k^{-1}-1)}{r_2Q_2}} \cdots\cdots (12)$$

where r_c is the core loss resistance, r_2 is the winding resistance of the secondary coil, and Q_1 and Q_2 are the quality factors of the primary and secondary coils, respectively. For example, when the calculated value of k deviates by −10% (0.288) from 0.320, the measured value, for a transmission

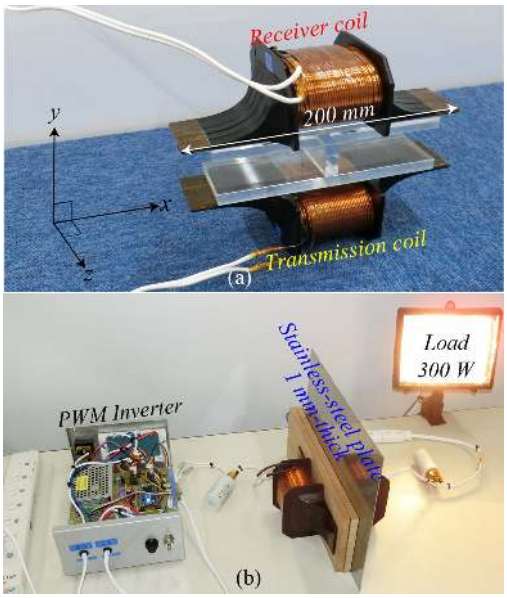

Fig. 3. Prototype P6 used in simulation: (a) Photograph of coils, (b) Demonstration of WPT through a stainless-steel plate (UNS S30400). When driven at 400 Hz, 80% efficiency and 317 W output were achieved when transmitting power through a 1 mm-thick UNS S30400 plate over a distance of 30 mm

Table 1. Specifications of prototype P6

Schematic drawings	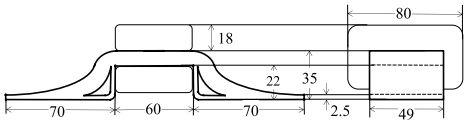	
Specifications	Weight	1.69 kg (Core 0.75 kg + Winding 0.94 kg)
	Magnet-pole area	70 × 49 (3,430) mm^2
	Cross-sectional area	13 × 49 (637) mm^2
	Winding diameter	1.5 mm
	Number of turns (layers)	360 turns (10)
	Space factor of a coil	58.9 %
	Thickness of silicon steel plate	0.10 mm
Coil parameters	Q factor	73.6 @ 400 Hz
	Winding resistance (r_1, r_2)	1.04 Ω @ 400 Hz
	Core loss resistance (r_c)	0.42 Ω @ 400 Hz
	Self-inductance	31.3 mH
	Coupling coefficient (k)	0.32 @ δ = 30 mm

distance of 30 mm, the calculated η deviates by 1.7% (89.6% vs. 91.3%). The calculation error of η propagates to the estimated output power, and thus a highly accurate computation of k is very important in the initial design stage. Although a high estimation accuracy is also required for Q, the self-inductance of the coil can be treated as a constant in this simulation and can be calculated using conventional methods, such as the permeance method. As for the calculation of k, since k cannot be treated as a constant value in a simulation in which the transmission distance fluctuates dynamically, the k values should be calculated continuously on time dimension. Among the parameters in Eq. (12), this computation process was required only for k.

Figures 4(a) to 4(c) show contour graphs of magnetic flux density for various d_{PML} values. The transmitter is at the bottom and the receiver is at the top. These simulations were carried out with the N value and $\sigma_{e,max}$ fixed at 5 and 1.0 S/m, respectively. A sinusoidal current source with a frequency of 400 Hz was connected to the transmission coil. In the original FDTD method, the instantaneous value at a particular time is output as the calculation result. However, all contour graphs shown here are based on the average values in half a cycle; the obtained trends are the same as those that would have been obtained if instantaneous values had been used. The material physical properties of the magnetic core and copper winding are required for the calculation. Here, nominal values given by the manufacturers were used.

For d_{PML} = 8 in Fig. 4(a), the bilateral symmetry of the magnetic field collapsed. The asymmetry was more pronounced for d_{PML} = 4. This violates Gauss's law, so it would not occur in reality. This asymmetry may be due to part of the magnetic flux emitted from one magnetic pole being blocked at the end of the analysis region, which would prevent it from returning to the magnetic pole pair. The symmetry improves with increasing d_{PML}, becoming almost ideal at a value of above 32. Of note, magnetic fluctuations appeared prominently when the PML was thicker than 32. These fluctuations are thought to be due to the degradation of the numerical stability in the PML. Numerical stability is discussed in detail in the next section.

Figure 5(a) shows the dependence of the k value on d_{PML}. The k value was calculated as a ratio of the magnetic

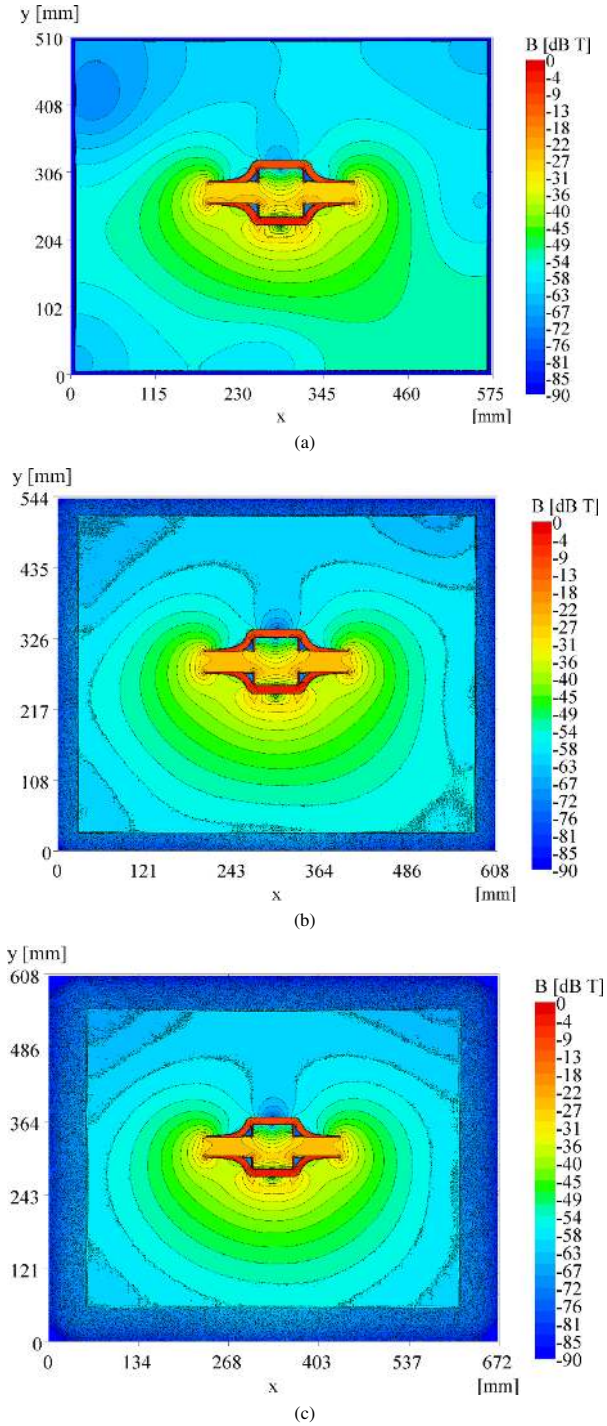

Fig. 4. Magnetic flux density distributions for B-PML. N = 5, $\sigma_{e,max}$ = 1.0 S/m, and (a) d_{PML} = 8, k = 0.291, (b) d_{PML} = 32, k = 0.309, and (c) d_{PML} = 64, k = 0.312

flux passing through the transmission coil and that passing through the receiver coil. For d_{PML} = 4, the k value was 0.272, which is greatly different from the measured value of 0.320. The k value approaches the measured value with increasing d_{PML}. It saturated at 0.312 at around 64 layers; however, the saturated value was slightly smaller than the measured value. We also simulated Mur's ABC for comparison with the PML [16], but the estimated k value was 0.188. Boundary conditions that manipulate the direction of wave propagation are thus not effective in the simulation.

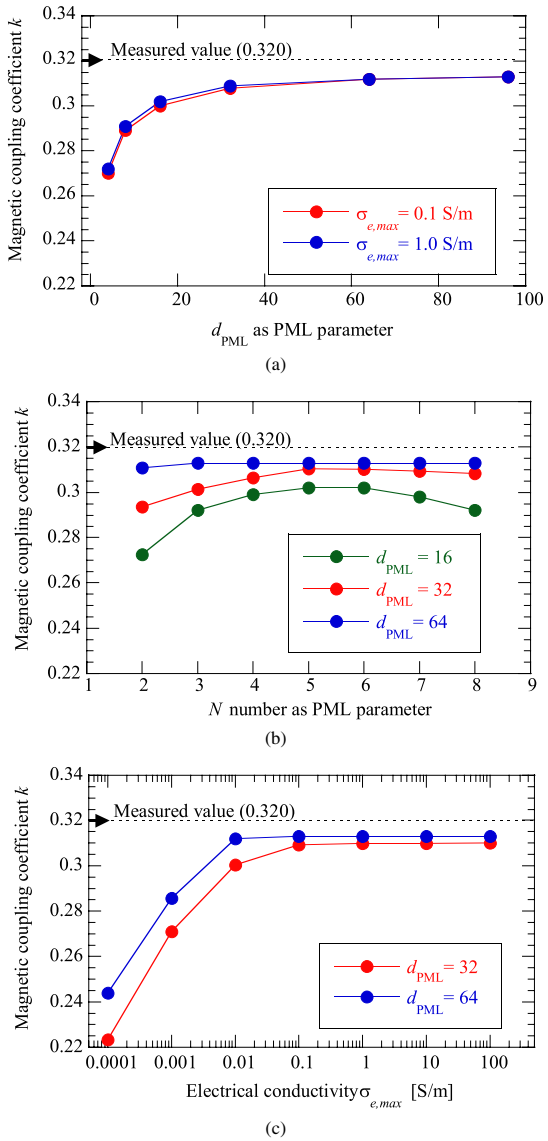

Fig. 5. Relationship between estimated k values and B-PML parameters. Data points are connected by straight lines for clarity. (a) Dependence of k on d_{PML}, with N fixed at 5. (b) Dependence of k on N, with $\sigma_{e,max}$ fixed at 1.0 S/m. (c) Dependence of k on $\sigma_{e,max}$, with N fixed at 5

Figure 5(b) shows the relationship between N and k values. When d_{PML} was less than 32 layers and N was set to a small value of 1 to 4, the estimated k values greatly differed from the experimental results. When N was small, σ_e became large near the boundary. It is thought that the magnetic field in the analysis region is affected when a large σ_e is used, and thus the k value could not be estimated accurately. However, for $d_{\mathrm{PML}} = 16$, the estimation accuracy was low even when N was large. For $d_{\mathrm{PML}} = 16$, when N exceeded 4, as that could be understood from the curves of σ_e in Fig. 2, the curve was similar to that obtained for a smaller d_{PML}. In such a case, the electric field intensity will not be sufficiently attenuated until the propagating wave reaches the end of the PML.

Figure 5(c) shows the relationship between the magnitude of $\sigma_{e,max}$ and the k value. To obtain a calculated value close to 0.320 (the measured value), it was necessary to set $\sigma_{e,max}$ above 0.1 S/m. When an external alternating magnetic field is applied in a direction perpendicular to the surface of a metal plate, since the penetration depth of the magnetic field depth depends on frequency [13], when the frequency changes, the $\sigma_{e,max}$ value should be changed appropriately.

An examination of B-PML parameters revealed that more than 64 layers are required for the PML; however, even when the PML conditions were properly set, the estimated k value (0.312) was still slightly smaller than the measured value (0.320).

3. Convolutional PML and Simulation Results

C-PML is an implementation of CFS-PML using recursive convolution [32]. C-PML was chosen here because the original CFS-PML proposed by Kuzuoglu and Mittra is only suitable for three-dimensional (3D) analysis [22]. In this section, we consider the origin of the fluctuations in the magnetic field and show that C-PML can effectively suppress these fluctuations. The Laplace transform was applied to Eqs. (4) and (5), the results of which were then summed to obtain the following equation:

$$j\omega\varepsilon_0\dot{E}_z = \frac{1}{\dot{s}_x}\frac{\partial\dot{H}_y}{\partial x} - \frac{1}{\dot{s}_y}\frac{\partial\dot{H}_x}{\partial y} \cdots\cdots (13)$$

where $\dot{E}_z$ is an expression in the frequency domain of E_z. The following function of the stretched-coordinate metric $\dot{s}_\varsigma$ was suggested by Berenger:

$$\dot{s}_\varsigma = 1 + \frac{\sigma_\varsigma}{j\omega\varepsilon_0}, \quad (\varsigma = x, y, \text{ or } z) \cdots\cdots (14)$$

Of note, σ_ς is $\sigma_{e\varsigma}$ for the Ampere-Maxwell equation and $\sigma_{m\varsigma}$ for Faraday's law. It is thought that the deterioration of numerical stability is related to Eq. (14). When waves near $\omega = 0$ are included, such as is done for a quasi-static magnetic field, $\dot{s}_\varsigma$ reaches infinity, and the link between the magnetic field and the electric field is cut, degrading the numerical stability in the B-PML.

For the C-PML, the stretched-coordinate metric is given as the Debye dispersion function [32]:

$$\dot{s}_\varsigma = \kappa_\varsigma + \frac{\sigma_\varsigma}{a_\varsigma + j\omega\varepsilon_0}, \quad (\varsigma = x, y, \text{ or } z) \cdots\cdots (15)$$

where a_ς is $a_{e\varsigma}$ (Ampere-Maxwell equation) or $a_{m\varsigma}$ (Faraday's law). Applying Eq. (15), the Ampere-Maxwell equation becomes

$$j\omega\varepsilon_0\frac{\dot{s}_x\dot{s}_y}{\dot{s}_z}\dot{E}_z = \frac{\partial\dot{H}_y}{\partial x} - \frac{\partial\dot{H}_x}{\partial y} \cdots\cdots (16)$$

Extending Eq. (16) to three dimensions yields

$$j\omega\varepsilon_0\bar{\bar{\dot{s}}}\dot{\boldsymbol{E}} = \nabla\times\dot{\boldsymbol{H}} \cdots\cdots (17)$$

Faraday's law can be expressed as

$$-j\omega\mu_0\bar{\bar{\dot{s}}}\dot{\boldsymbol{H}} = \nabla\times\dot{\boldsymbol{E}} \cdots\cdots (18)$$

where tensor $\bar{\bar{\dot{s}}}$ of the stretched coordinate is expressed as follows:

$$\bar{\bar{\dot{s}}} = \begin{bmatrix} \dfrac{\dot{s}_y\dot{s}_z}{\dot{s}_x} & 0 & 0 \\ 0 & \dfrac{\dot{s}_y\dot{s}_z}{\dot{s}_y} & 0 \\ 0 & 0 & \dfrac{\dot{s}_x\dot{s}_y}{\dot{s}_z} \end{bmatrix} \cdots\cdots (19)$$

By introducing a_ς, the coordinates of the real space are extended, so that it is possible to attenuate the evanescent waves that were barely attenuated in the B-PML [23]. We expected the numerical stability to improve for the C-PML because s_ς does not reach infinity due to the presence of a_ς, even around $\omega = 0$.

When Eq. (15), proposed by Roden et al. [32], is used in place of Eq. (14), the electric conductivity and magnetic conductivity in the absorption layer can be described by a Debye dispersion function. However, with this change, it is necessary to specify appropriate values for the new parameters κ_ς and a_ς. Therefore, Eq. (15) is modified as:

$$s_\varsigma = 1 + \frac{\sigma_\varsigma}{\gamma\sigma_\varsigma + j\omega\varepsilon_0}, \quad (\varsigma = x, y, \text{ or } z) \cdots\cdots\cdots (20)$$

In Eq. (20), κ_ς and a_ς are omitted, and proportionality constant γ is introduced. It is thought that this will improve numerical stability since s_ς does not reach infinity, even around $\omega = 0$, if γ is set to a finite value. An appropriate value of γ must be determined.

For a parallel polarized TM wave propagating through a 2D analysis area, Eqs. (17) and (18) can be transformed into difference equations that follow Yee's scheme, yields Eqs. (21) to (23). Comparing these equations with the B-PML difference equations shown in Eqs. (6) to (9), only the one-dimensional α_ς and β_ς functions were added. When B-PML was replaced with C-PML, the usage of GPU memory only slightly increased, remaining near 27%.

Figure 6 shows a contour graph for $r = 0.005$. The numerical stability was dramatically improved by introducing the C-PML. To show the difference between the B-PML and the C-PML, vector diagrams of the corresponding magnetic fields are shown in Figs. 7(a) and 7(b), respectively. These vector diagrams are enlarged views of the broken-line rectangle in Fig. 6. For B-PML, the magnetic fields inside the PML and around the boundaries are oriented in random directions, whereas for C-PML, the fields are aligned.

Figure 8 shows a graph of the magnetic field intensities along line segment A-B in Fig. 7. The B-PML did not sufficiently attenuate the magnetic field, whereas the C-PML was

$$E_z^{n+1}(i,j) = \left(\frac{1-\frac{\sigma_{ex}(i)}{2\varepsilon_0}\Delta t}{1+\frac{\sigma_{ex}(i)}{2\varepsilon_0}\Delta t}\right)E_z^{n}(i,j) + \left(\frac{\frac{\Delta t}{\varepsilon_0}}{1+\frac{\sigma_{ex}(i)}{2\varepsilon_0}\Delta t}\right)\left[\frac{1}{\Delta x}\left(H_y^{n+\frac{1}{2}}\left(i+\frac{1}{2},j\right) - H_y^{n+\frac{1}{2}}\left(i-\frac{1}{2},j\right)\right)\right.$$
$$\left. -\frac{1}{\Delta y}\left(H_x^{n+\frac{1}{2}}\left(i,j+\frac{1}{2}\right) - H_x^{n+\frac{1}{2}}\left(i,j-\frac{1}{2}\right)\right) + \left(\Psi_{ezx}^{n+\frac{1}{2}}(i,j) - \Psi_{ezy}^{n+\frac{1}{2}}(i,j)\right)\right] \cdots\cdots (21)$$
$$\Psi_{exz}^{n+\frac{1}{2}}(i,j) = \beta_{ex}(i)\Psi_{exz}^{n-\frac{1}{2}}(i,j) + \frac{\alpha_{ex}(i)}{\Delta x}\left[H_y^{n+\frac{1}{2}}\left(i+\frac{1}{2},j\right) - H_y^{n+\frac{1}{2}}\left(i-\frac{1}{2},j\right)\right]$$
$$\Psi_{eyz}^{n+\frac{1}{2}}(i,j) = \beta_{ey}(j)\Psi_{eyz}^{n-\frac{1}{2}}(i,j) + \frac{\alpha_{ey}(j)}{\Delta y}\left[H_x^{n+\frac{1}{2}}\left(i,j+\frac{1}{2}\right) - H_x^{n+\frac{1}{2}}\left(i,j-\frac{1}{2}\right)\right]$$

where,

$$\left.\begin{aligned}\alpha_{e\varsigma}(\varsigma) &= \frac{\beta_{e\varsigma}(\varsigma)}{1+r}\\ \beta_{e\varsigma}(\varsigma) &= \exp\left[-\sigma_{e\varsigma}(\varsigma)(1+r)\frac{\Delta t}{\varepsilon_0}\right]\end{aligned}\right\}\ \varsigma \text{ indicate } x \text{ and } i, \text{ or } y \text{ and } j$$

$$H_x^{n+\frac{1}{2}}\left(i,j+\frac{1}{2}\right) = \left(\frac{1-\frac{\sigma_{my}(j)}{2\mu_0}\Delta t}{1+\frac{\sigma_{my}(j)}{2\mu_0}\Delta t}\right)H_x^{n-\frac{1}{2}}\left(i,j+\frac{1}{2}\right) - \left(\frac{\frac{\Delta t}{\mu_0}}{1+\frac{\sigma_{my}(j)}{2\mu_0}\Delta t}\right)\left[\frac{1}{\Delta y}\left(E_z^{n}(i,j+1) - E_z^{n}(i,j)\right) + \Psi_{hxy}^{n}(i,j)\right] \cdots\cdots (22)$$

$$H_y^{n+\frac{1}{2}}\left(i+\frac{1}{2},j\right) = \left(\frac{1-\frac{\sigma_{mx}(i)}{2\mu_0}\Delta t}{1+\frac{\sigma_{mx}(i)}{2\mu_0}\Delta t}\right)H_y^{n-\frac{1}{2}}\left(i+\frac{1}{2},j\right) + \left(\frac{\frac{\Delta t}{\mu_0}}{1+\frac{\sigma_{mx}(i)}{2\mu_0}\Delta t}\right)\left[\frac{1}{\Delta x}\left(E_z^{n}(i+1,j) - E_z^{n}(i,j)\right) + \Psi_{hyx}^{n}(i,j)\right] \cdots\cdots (23)$$

$$\Psi_{hxy}^{n}(i,j) = \beta_{my}(j)\Psi_{hxy}^{n-1}(i,j) + \frac{\alpha_{my}(j)}{\Delta y}\left[E_z^{n}(i,j+1) - E_z^{n}(i,j)\right]$$

$$\Psi_{hyx}^{n}(i,j) = \beta_{mx}(i)\Psi_{hyx}^{n-1}(i,j) + \frac{\alpha_{mx}(i)}{\Delta x}\left[E_z^{n}(i+1,j) - E_z^{n}(i,j)\right]$$

where,

$$\left.\begin{aligned}\alpha_{m\varsigma}(\varsigma) &= \frac{\beta_{m\varsigma}(\varsigma)}{1+r}\\ \beta_{m\varsigma}(\varsigma) &= \exp\left[-\sigma_{m\varsigma}(\varsigma)(1+r)\frac{\Delta t}{\mu_0}\right]\end{aligned}\right\}\ \varsigma \text{ indicate } x \text{ and } i, \text{ or } y \text{ and } j$$

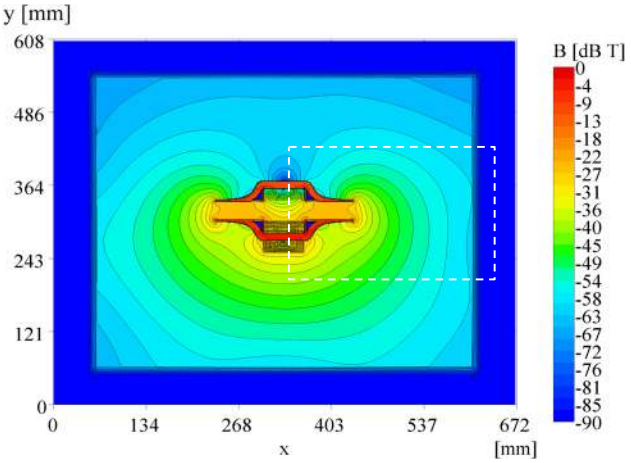

Fig. 6. Magnetic flux density distribution for introducing C-PML

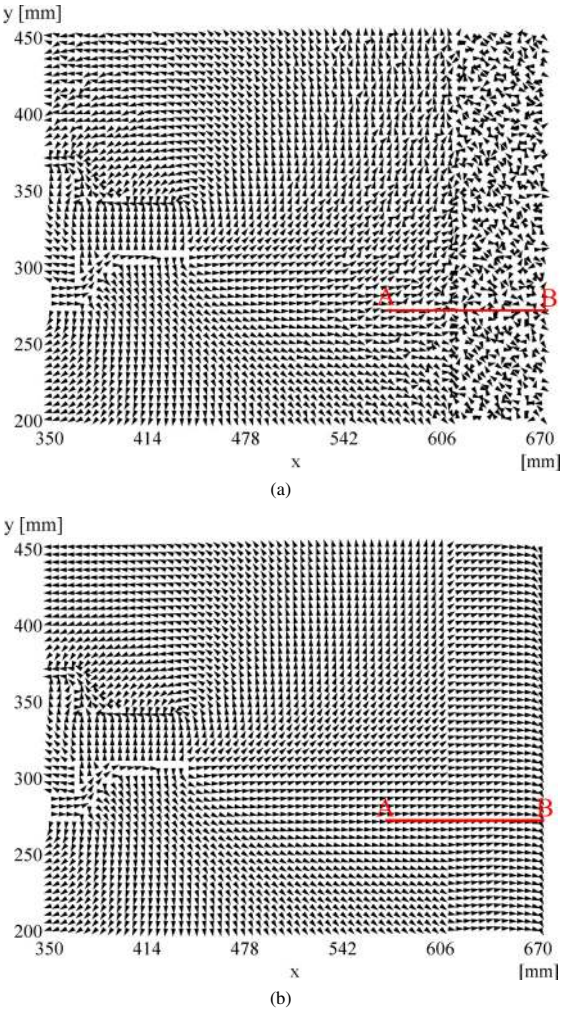

Fig. 7. Vector diagrams of magnetic field with (a) B-PML and (b) C-PML. These vector diagrams are enlarged views of the broken-line rectangle in Fig. 6

able to. This is a well-known characteristic of the C-PML for low-frequency electromagnetic fields [22]. The estimation accuracy of the k value when the C-PML is used is important. Figure 9 shows the dependence of the k value on d_{PML}. For the C-PML, k saturated at 0.319, which is very close to the measured value (0.320). The r value affected the gradient of

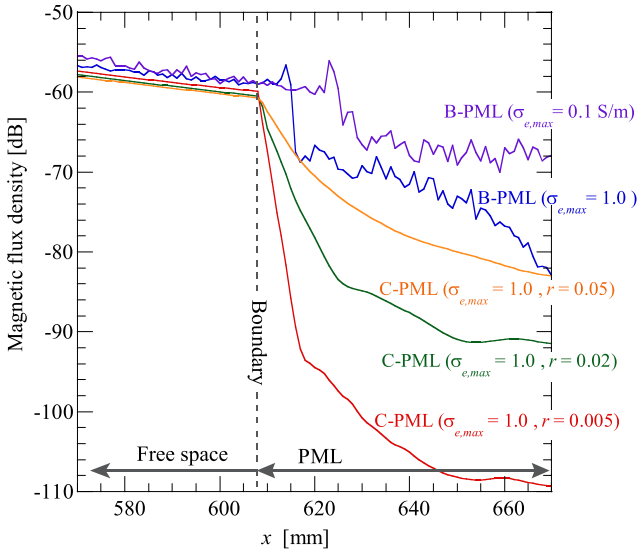

Fig. 8. Magnetic fluctuations generated around PML boundary

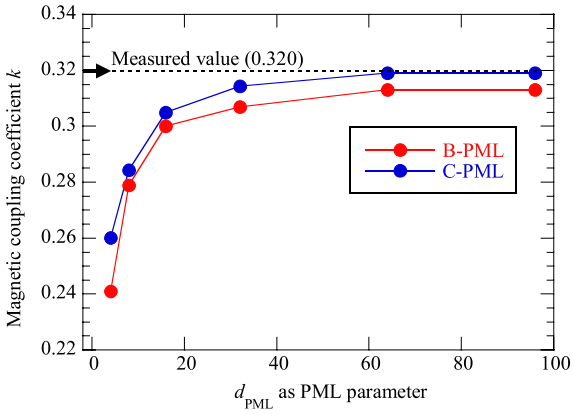

Fig. 9. Comparison of estimation accuracy of k for B-PML and C-PML, in this graph, r was fixed at 0.005

magnetic field attenuation, but it had almost no effect on the estimated k value value when r values was below 0.01.

These simulation results show that introducing the C-PML is useful for estimating the k value with high accuracy. However, as transmission distance increases, the magnetic field spreads out, so it is necessary to confirm whether the k value can be accurately estimated for a given transmission distance. Figure 10 shows the dependence of the k value on transmission distance. Here, d_{PML} was fixed at 64 layers. The calculation results obtained with the C-PML are in good agreement with experimental data for short transmission distances (less than 40 mm); the values diverge for larger transmission distances. The average error between experimental data and calculation results for distances of up to 40 mm was 3.9%.

Taking practical applications into consideration, it is necessary to investigate the effects of lateral displacement between the two coils on the estimated k value. Figure 11 show the variation in k values with lateral displacement. Here, the transmission distance was fixed at 30 mm. The experiment was performed by horizontally moving the receiver coil in the range of ±70 mm. The calculation results obtained with the C-PML are in good agreement with experimental data for small displacements. The results in Figs. 10 and 11 show that

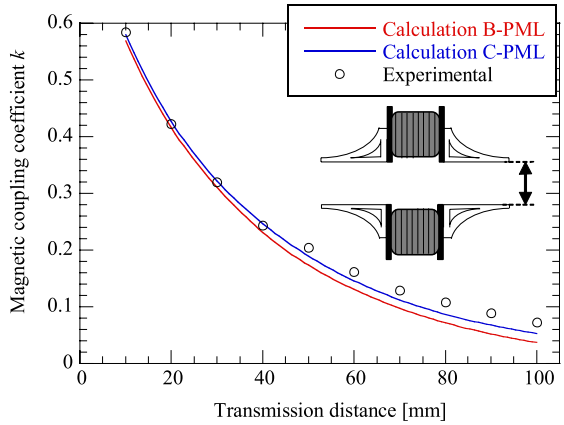

Fig. 10. Dependence of k on transmission distance

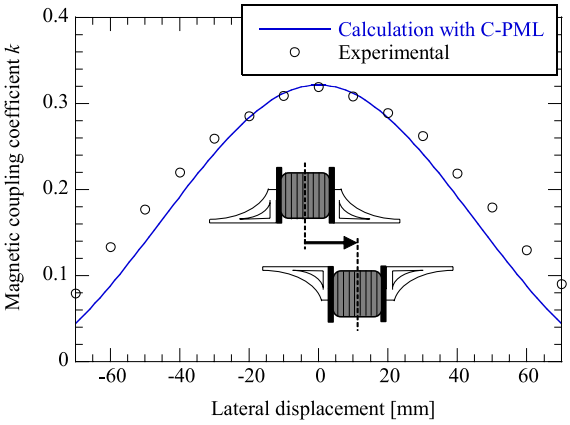

Fig. 11. Dependence of k on lateral displacement

the simulation becomes less accurate when the coupling between the coils becomes weaker. When the coupling is weak, the leakage magnetic field will spread over a wide area. If the analysis area is increased, the magnetic field spread can be included in the calculations, improving the estimation accuracy of k. Unfortunately, we could not expand the analysis area further due to the performance limit of the GPU used for calculations. For simulating a WPT system with a k value of below 0.1, a faster GPU is required.

The simulations were conducted using a 2D analysis area. The reason why the estimated values of k had high accuracy may be the specific shape of the magnetic core. For the applied magnetic core, the magnetic field spreading in the z direction may have been much weaker than that in the x-y plane, and thus the k values were estimated without considering the z direction. To further improve estimation accuracy, 3D analysis should be done. This has not been done yet due to the limits of our computational resources, as such a simulation would require at least hundreds of GPUs.

4. Conclusion

Two types of PML were applied in a WPT simulation based on FDTD. Effectiveness was evaluated in terms of the calculation accuracy of k values. Although the B-PML is an effective ABC for WPT simulation, numerical stability and the attenuation of magnetic fields are problems. The C-PML solves these problems. Furthermore, the estimation accuracy of the k value was improved by introducing the C-PML. This was due to the use of a stretched-coordinate metric with the Debye dispersion function. The results are useful for the time-domain magnetic field analysis of magnetic-resonance-type WPT.

Acknowledgment

This research was supported in part by Japan Society for the Promotion of Science KAKENHI Grant Number 18K04115.

References

(1) B.L. Cannon, J.F. Hoburg, D.D. Stancil, and S.C. Goldstein: "Magnetic resonant coupling as a potential means for wireless power transfer to multiple small receivers", *IEEE Trans. Power Electron.*, Vol.24, pp.1819–1826 (2009)

(2) T.C. Beh, M. Kato, T Imura, S. Oh, and Y. Hori: "Automated impedance matching system for robust wireless power transfer via magnetic resonance coupling", *IEEE Trans. Ind. Electron.*, Vol.60, pp.3689–3698 (2013)

(3) S. Assawaworrarit, X. Yu, and S. Fan: "Robust wireless power transfer using a nonlinear parity-time-symmetric circuit", *Nature*, Vol.546, pp.387–390 (2017)

(4) A. Sample, D. Meyer, and J. Smith: "Analysis, experimental results, and range adaptation of magnetically coupled resonators for wireless power transfer", *IEEE Trans. Ind. Electron.*, Vol.58, pp.544–554 (2011)

(5) M.J. Jenkinson and J.W. Banks: "High-order accurate FDTD schemes for dispersive Maxwell's equations in second-order form using recursive convolutions", *Journal of Computational and Applied Mathematics*, Vol.336, pp.192–218 (2018)

(6) W. Bao and F.L. Teixeira: "Performance analysis of perfectly matched layers applied to spherical FDTD grids", *IEEE Trans. Ant. Prop.*, Vol.66, pp.1035–1039 (2018)

(7) A. Christ, M.G. Douglas, J.M. Roman, E.B. Cooper, A.P. Sample, B.H. Waters, J.R. Smith, and N. Kuster: "Evaluation of wireless resonant power transfer systems with human electromagnetic exposure limits", *IEEE Trans. Electromagn. Compat.*, Vol.55 pp.265–274 (2013)

(8) Y. Li, L. Zhu, and J. Zhu: "Core loss calculation based on finite-element method with Jiles–Atherton dynamic hysteresis model", *IEEE Trans. Magn.*, Vol.54, No.1300105 (2018)

(9) M. Shafieipour, Z. Chen, A. Menshov, J.D. Silva, and V. Okhmatovski: "Efficiently computing the electrical parameters of cables with arbitrary cross-sections using the method-of-moments", *Electric Power Systems Research*, Vol.162, pp.37–49 (2018)

(10) R. Courant, K. Friedrichs, and H. Lewy: "On the partial difference equations of mathematical physics", *IBM Journal of Research and Development*, Vol.11, pp.215–234 (1967)

(11) M.R. Zunoubi, J. Payne, and W.P. Roach: "CUDA implementation of TE^z-FDTD solution of Maxwell's equations in dispersive media", *IEEE Antennas and Wireless Propagation Letters*, Vol.9, pp.756–759 (2010)

(12) H. Ishida, H. Furukawa, T. Kyoden, and T. Tanaka: "Development of a wireless power transmission simulator based on finite-difference time-domain using graphics accelerators", *IET Power Electron.,* Vol.10, pp.1889–1895 (2017)

(13) H. Ishida, T. Kyoden, and H. Furukawa: "Super-low-frequency wireless power transfer with lightweight coils for passing through a stainless steel plate", *Rev. Sci. Instrum.*, Vol.89, 034706 (2018)

(14) International Commission of Non-ionizing Radiation: "Guidelines for limiting exposure to time-varying electric and magnetic fields (1 Hz to 100 kHz)", *Health Physics*, Vol.100, pp.818–836 (2011)

(15) J.P. Berenger: "A perfectly matched layer for the absorption of electromagnetic waves", *J. Comput. Physics,* Vol.114, pp.185–200 (1994)

(16) G. Mur: "Absorbing boundary conditions for the finite-difference approximation of the time domain electromagnetic field equations", *IEEE Trans. Electromagn. Compat.*, Vol.23, pp.277–382 (1981)

(17) R.L. Higdon: "Absorbing boundary conditions for difference approximations to the multi-dimensional wave equation", *Math. Comp.*, Vol.47, pp.437–459 (1986)

(18) Z.P. Liao, H.L. Wong, B.P. Yang, and Y.F. Yuan: "A transmitting boundary for transient wave analysis", *Science Sinica, Series A*, Vol.27, pp.1063–1076 (1984)

(19) B. Nikolic, B. Dimitrijevic, S. Aleksic, and N. Raicevic: "Improved direct radiation pattern estimation in FDTD", *Electronics Letters*, Vol.53, pp.60–62 (2017)

(20) I. Giannakis, A. Giannopoulos, and C. Warren: "A realistic FDTD numerical modeling framework of ground penetrating radar for landmine detection",

IEEE Journal of Selected Topics in Applied Earth Observations and Remote Sensing, Vol.9, pp.37–51 (2015)
(21) J.P. Berenger: "Perfectly matched layer for the FDTD solution of wave-structure interaction problems", *IEEE Trans. Ant. Prop*., Vol.44, pp.110–117 (1996)
(22) M. Kuzuoglu and R. Mittra: "Frequency dependence of the constitutive parameters of causal perfectly matched anisotropic absorbers", *IEEE Microwave and Guided Wave Letters*, Vol.6, pp.447–449 (1996)
(23) J.P. Berenger: "Application of the CFS PML to the absorption of evanescent waves in waveguides", *IEEE Microwave and Wireless Components Letters*, Vol.12, pp.218–220 (2002)
(24) K. Sugahara: "Electromagnetic analysis of wireless power transfer system with improvised absorbing boundary conditions", in Proceedings of Progress in Electromagnetic Research Symposium, pp.1152–1155 (2016)
(25) H. Ishida and H. Furukawa: "Wireless power transmission through concrete using circuits resonating at utility frequency of 60 Hz", *IEEE Trans. Power Electron.*, Vol.30, pp.1220–1229 (2014)
(26) K. Shimamura and K. Komurasaki: "Wireless power transmission into metallic tube using axial slit for infrastructure diagnostics", *Wireless Engineering and Technology*, Vol.6, pp.50–60 (2015)
(27) T. Tohi, Y. Kaneko, and S. Abe: "Maximum efficiency of contactless power transfer systems using k and Q", *IEEJ Trans. Industry Applications*, Vol.132, pp.123–124 (2012) (in Japanese)
(28) H. Ishida, H. Furukawa, and T. Kyoden: "Development of design methodology for 60 Hz wireless power transmission system", *IEEJ Journal of Industry Applications*, Vol.5, pp.429–438 (2016)
(29) P. Sypek, A. Dziekonski, and M. Mrozowski: "How to render FDTD computations more effective using a graphics accelerator", *IEEE Trans. Magn.*, Vol.45, pp.1324–1327 (2009)
(30) T. Uno: "Finite difference time domain method for electromagnetic field and antennas", Corona Pub. Co. Ltd. (1998) (in Japanese)
(31) K. Yee: "Numerical solution of initial boundary value problems involving Maxwell's equations in isotropic media", *IEEE Trans. Ant. Prop.*, Vol.14, pp.302–307 (1966)
(32) J.A. Roden and S.D. Gedney: "Convolution PML (CPML): An efficient FDTD implementation of the CFS-PML for arbitrary media", *Microwave Opt. Technol. Lett.*, Vol.27, pp.334–339 (2000)

Hiroki Ishida (Member) received the Ph.D. degree in electrical engineering from Nagaoka University of Technology, Nigata, Japan, in 2004. He joined Okayama University of Science as an associate professor in the Department of Applied Physics, in 2015. His current research interests include wireless power transmissions. He is a member of the IEEJ and the IEEE.

Tomoaki Kyoden (Member) received the Ph.D. degree in mechanical Engineering from Kanazawa University, Ishikawa, Japan, in 2014. He joined the National Institute of Technology, Toyama College, in 2010, and has been an associate professor there since 2017. His current reserch interests include focus on energy conversion high-efficiency technology and utilization of renewable energy. He is a member of the IEEJ.

Hiroto Furukawa (Member) received the M.S. degree in electrical engineering from Tokyo Denki University, Tokyo, Japan, in 1989. He joined the National Institute of Technology, Toyama College, in 1991, and has been an associate professor there since 2003. He has been engaged in propagation characteristics of microwave. He is a member of the IEEJ.